Corrosion Science 90 (2015) 46–53

Contents lists available at ScienceDirect

Corrosion Science

journal homepage: www.elsevier.com/locate/corsci

Corrosion behaviour of stainless steels and a single crystal superalloy in a ternary LiCl–KCl–CsCl molten salt

M. Hofmeister [a], L. Klein [b], H. Miran [a], R. Rettig [a], S. Virtanen [b,*], R.F. Singer [a]

[a] Department of Materials Science and Engineering, Institute of Metals Science and Technology (WTM), Martensstr. 5, Friedrich-Alexander-University Erlangen-Nürnberg, 91058 Erlangen, Germany
[b] Department of Materials Science and Engineering, Institute for Surface Science and Corrosion (LKO), Martensstr. 7, University of Erlangen-Nuremberg, 91058 Erlangen, Germany

ARTICLE INFO

Article history:
Received 12 August 2014
Accepted 15 September 2014
Available online 2 October 2014

Keywords:
A. Stainless steel
A. Superalloys
A. Molten salts
B. XPS
C. Intergranular corrosion
C. Passivity

ABSTRACT

In the present work, the corrosion properties of a low-carbon stainless steel (X2CrNi18–9) and a Ti-stabilised high-carbon stainless steel (X6CrNiTi18–10) were investigated in a molten LiCl–KCl–CsCl salt at 400, 500, and 600 °C for 1, 3, 9 and 27 h. In addition, a Ni-based superalloy (CMSX-4) was tested at 800 °C for 3 h. The low-carbon steel revealed severe intergranular corrosion for all testing conditions, whereas the Ti-stabilised steel was protected against intergranular corrosion by a Cr_2O_3 passive layer for short exposure times and up to a temperature of approximately 500 °C. In comparison, CMSX-4 revealed superior corrosion resistance.

© 2014 Elsevier Ltd. All rights reserved.

1. Introduction

Molten salts are widely applied as heat transfer media in high temperature applications. Examples are fluoride salts in nuclear power plant concepts [1], alkali metal nitrates and nitrites and their mixtures in solar energy power plants or cyanates for heat treatment processes of steels [2,3]. We are presently evaluating whether molten salts are also suitable for cooling baths in the directional solidification of turbine blades made from nickel-based superalloys (liquid salt cooling (LSC) casting process).

All directional solidification processes aim for the temperature gradient between the hot and the cold zone to be as high as possible. High gradients are desired because they allow for higher withdrawal rates and reduced cost. Moreover, they lead to finer microstructures, in particular smaller dendrite arm spacings and pores, which shortens heat treatment times and improves mechanical properties (fatigue, creep) [4,5]. State of the art is the Bridgman process based on radiation cooling with a rather small temperature gradient, while new processes like liquid metal cooling (LMC) with larger gradients using tin and aluminium baths have been developed [6]. Although the advantages of LMC are well documented, the process suffers from a number of disadvantages that may be overcome by using molten salts as a cooling bath. Attack of the casting surface from the liquid metal in mould failure situations is being one.

The conditions in a LSC casting process are very demanding and the selection of suitable salts is anything but straightforward. Especially critical is a shell mould failure under conditions early on in the process, when the nickel-melt with temperatures around 1550 °C will come in contact with the molten salt. Many salts show under such conditions strong exothermal reactions with metal melts and cannot be used.

Halide salts are favourable at high temperatures because they possess very good thermal stability. Fluorides are chosen for instance in nuclear heat transfer devices [1,7]. Compared to chlorides, fluorides are known to be more toxic and they tend to form HF at high temperatures. From that point of view, a low melting chloride salt eutectic like LiCl–CsCl–KCl is a promising candidate for the cooling media in the LSC process, even if the vapour pressure is somewhat higher than for fluorides [8].

Salt mixtures show an inhomogeneous rate of evaporation. The species with the highest vapour pressure evaporates most rapidly [9]. The selective evaporation results in a change of thermo-physical properties. The evaporation is controlled by temperature and increases with decreasing pressure. In order to avoid an excessive rate of evaporation, LSC casting processes have to be operated in an inert gas atmosphere.

Literature suggests that the corrosivity of molten chlorine salts is mostly controlled by the oxygen and water adsorbed in the salt

* Corresponding author. Tel.: +49 9131 8527577; fax: +49 9131 8527582.
E-mail addresses: matthias.hofmeister@fau.de (M. Hofmeister), leonhard.klein@ww.uni-erlangen.de (L. Klein), hossein.miran@gmail.com (H. Miran), ralf.rettig@fau.de (R. Rettig), virtanen@ww.uni-erlangen.de (S. Virtanen), robert.singer@ww.uni-erlangen.de (R.F. Singer).

http://dx.doi.org/10.1016/j.corsci.2014.09.009
0010-938X/© 2014 Elsevier Ltd. All rights reserved.

[10]. Furthermore, LiCl and CsCl are highly deliquescent [11,12]. Oxidants do not only originate from the environment but some (O_2, H^+, H_2O and OH^-) are commonly present in the molten salts and may form during the dissociation reaction at elevated temperature [10]. To receive "non corrosive" conditions, a pre-treatment is necessary. Drying under vacuum followed by prolonged treatment with dry HCl gas and an inert gas purge is recommended [11,12]. Nevertheless, some bound oxygen may remain in the salt [8]. It is important to point out that the effort and result of the pre-treatment is lost as soon as the salt is exposed again to the environment [11]. For an industrial scale casting process, some hundred kilograms of salt are necessary, which makes pre-treatment and its conservation complex and challenging. In the following, in order to meet realistic conditions, the experiments are conducted with salt that has been dried under vacuum solely.

Common construction materials for procedural devices are chromia forming stainless steels. Nickel matrices, in particular when alumina forming, are reported to be better performing in fused salts especially if oxygen is present [13]. On the other hand, chromia formers may be resistant if the atmosphere is controlled, i.e., contact to air and moisture is prevented [14].

Intergranular corrosion is the typical corrosion pattern in molten salts [14,15]. Durability for intergranular corrosion may be achieved by limitation of carbon content or stabilisation with carbide formers [14,16]. Based on these considerations, in the present paper the corrosion of typical structural materials (X2CrNi18–9 and X6CrNiTi18–10) as well as a typical single crystal superalloy (CMSX-4) by a eutectic chlorine salt mixture (LiCl–CsCl–KCl) will be investigated.

According to thermodynamic calculations with FactSage-software [17], a very low melting eutectic at 246 °C can be found for the following LiCl–KCl–CsCl mixture: 50.6 mol-% – 22.5 mol-% – 26.9 mol-%. This is comparable to the melting point of Sn (232 °C) currently used as cooling medium in the LMC process and therefore this composition will be used throughout the study.

2. Experimental method

2.1. Material preparation

The single mixture species were acquired from Rockwell Lithium (CsCl 99.999%), Carl Roth GmbH + Co. KG (KCl 99.5%) and Merck KGaA (LiCl ⩾ 99.0%), respectively. The as-delivered salts were ground in a mortar to a floury state at ambient conditions. Subsequently, the individual species were introduced into a glove box equipped with a vacuum furnace. The atmosphere inside the box was composed of N_2, and O_2 and H_2O were controlled to be below 1 ppm. The salt species were dried individually at 180 °C for 24 h and at a pressure below 4.8×10^{-1} mbar. Mixing was based on the weight percentage of each component. Afterwards, the ternary eutectic salt mixture was kept inside the glove box until starting the corrosion experiment. For each corrosion experiment, 150 g of the prepared ternary salt was required.

For the corrosion studies cylindrical metal specimens were prepared with an outer diameter of 12.0 mm. The bottom surface of each specimen was ground up to grade 4000 (SiC, STRUERS GmbH). Afterwards the specimens were ultrasonically cleaned in distilled water and ethanol. The compositions of the used stainless steels are given in Table 1. In addition, the nickel-based superalloy CMSX-4 was also investigated by dynamic corrosion experiments. The specimen was prepared similar to the stainless steels. However, it differed in the outer diameter (11.6 mm). The composition of the nickel-base material used in this study is provided in Table 1, as well. A typical prepared specimen with its polished bottom surface for dynamic corrosion experiments is shown in Fig. 1.

2.2. Experimental procedure

2.2.1. Evaporation

As is illustrated in Fig. 2, the mass loss during heating was performed in a thermogravimetric analysis (TGA, Netzsch STA 409 CD) with a heating rate of 1 K/min at ambient pressure.

2.2.2. Molten salt corrosion

The molten salt corrosion experiments were performed dynamically; the device is illustrated in Fig. 3. During the experiment, the metal specimen was rotated around its cylindrical axis in the fused salt in order to create shear flow in the bath and to achieve a uniform and reproducible flow pattern. The testing device was contained in a vertical tube furnace. A metal specimen was mounted on a rod aligned with a salt filled porcelain crucible (VWR Cat. Nr. 459-0214). In order to control the atmosphere, the crucible was placed in a tube vessel heated from outside by the furnace. Bellow elements allowed the axial adjustment of the specimen. The experiments can be carried out either under vacuum or protective argon atmosphere. For this study, the experiments were performed under argon (technical quality 4.6) atmosphere. The temperature inside the crucible was controlled to within ±2 K.

In order to achieve reproducible conditions, experiments started with a homogenisation step by waiting for 1 h as soon as the experiment temperature was achieved. Afterwards, the specimen was lowered into the molten salt and stirring was started at constant revolution number. After finishing the experiment, the motor and heating were switched off and the setup was kept under argon atmosphere during cool down. Finally the specimen could be disassembled and ultrasonically cleaned in distilled water and ethanol before drying. Cleaning was necessary in order to remove the salt crust from the surface of the specimen. A loss of certain corrosion products due to that procedure was tolerated. Otherwise, unacceptable pollution of the analytical equipment and chloride induced wet corrosion of the samples would have had to be expected. In the present study, three dynamic corrosion experiments for X2CrNi18–9, twelve (+ four additional for assessment) experiments for X6CrNiTi18–10 and one experiment on the nickel-base superalloy CMSX-4 were conducted. Table 2 summarises the details of the experiments.

2.2.3. Characterisation methods

After performing the molten salt corrosion experiments, the specimens were evaluated with respect to change in weight and

Table 1
Chemical compositions of the austenitic stainless steels (X2CrNi18–9, X6CrNiTi18–10) and the nickel-based superalloy CMSX-4.

	Measured composition, wt.-%																	
	C	P	S	Si	Mn	Cr	Mo	Ti	N	Cu	Co	Ta	Hf	W	Al	Re	Ni	Fe
X2CrNi18–9[1]	0.030	0.022	0.030	0.362	1.276	18.15	0.204	0.002	0.086	0.301	–	–	–	–	–	–	8.00	Bal.
X6CrNiTi18–10[2]	0.050	0.049	0.041	0.505	1.540	17.63	0.364	0.277	0.034	0.277	0.145	–	–	–	–	–	9.28	Bal.
CMSX–4[2]	0.031	–	0.007	0.119	0.028	6.52	0.661	0.986	0.041	0.041	8.33	6.63	0.097	6.56	5.89	2.73	Bal.	0.041

[1] According to material's certificate ("ROLDAN, S.A. – 3.1 EN 10204").
[2] Measured in-house with Spectromaxx LMX06, SPECTRO Analytical Instruments GmbH.

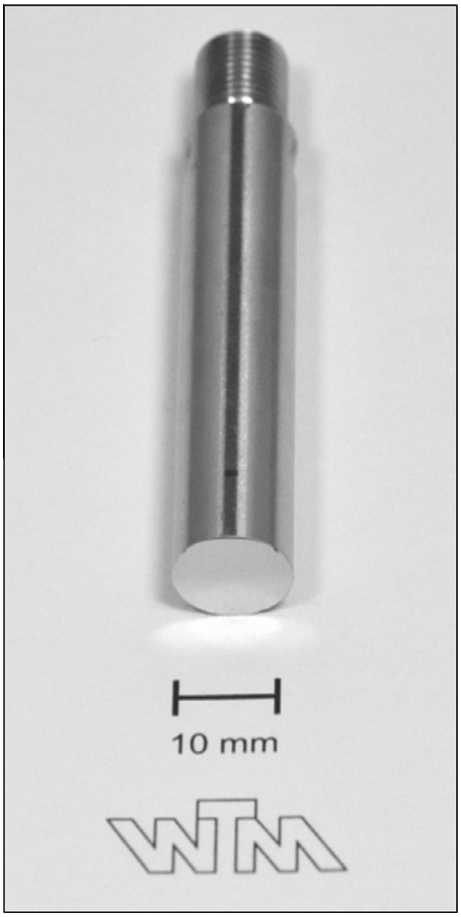

Fig. 1. Prepared X6CrNiTi18–10 specimen with the polished bottom surface for dynamic corrosion experiments.

diameter. Subsequently the samples were prepared for further characterisation. For this, approximately 5 mm thick pieces were cut off to investigate the initially ground bottom surface. A further set of specimens for microscopic analysis was obtained by cutting off additional three pieces from the bottom end of a single rod. Those samples were hot embedded in epoxy resin and again ground and polished. Subsequently, the specimens had to be cleaned with ethanol (and isopropanol for XPS investigations) in order to remove residues form the sample surface.

X-ray photoelectron spectra (XPS) were measured at an energy of 187.85 eV (0.8 eV resolution) on a high-resolution X-ray photoelectron spectrometer (Perkin Elmer, Physical Electronics PHI

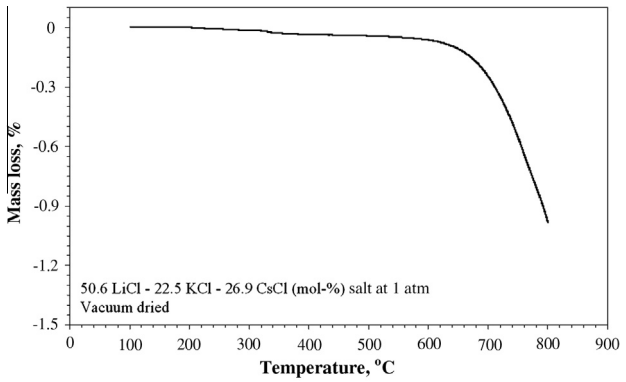

Fig. 2. Thermogravimetric analysis (TGA) of the ternary vacuum dried 50.6 LiCl–22.5 KCl–26.9 CsCl (mol-%) salt at 1 atm.

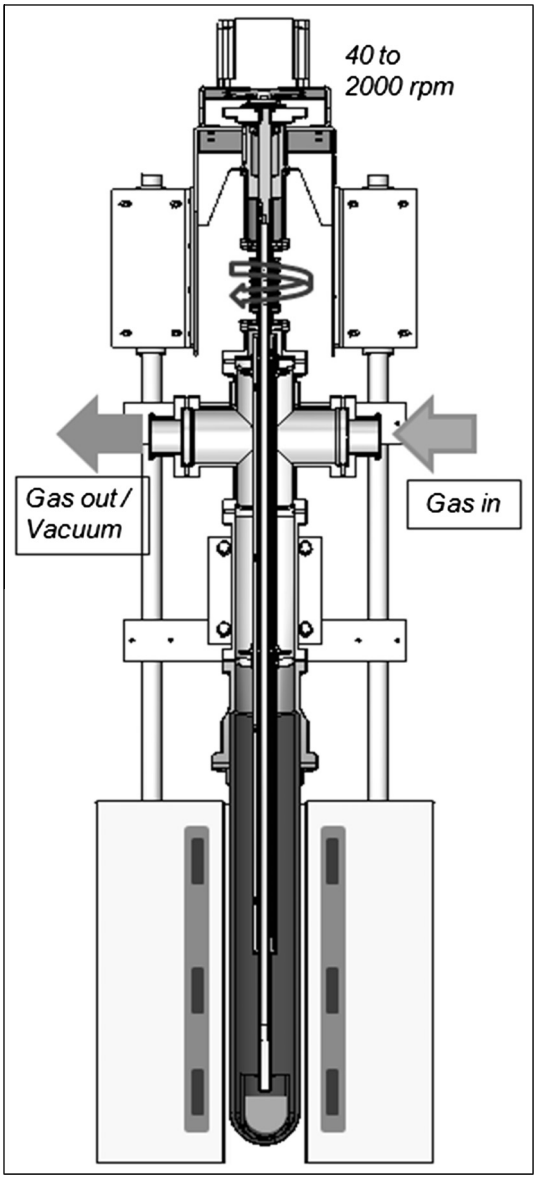

Fig. 3. Schematic drawing of the test apparatus for dynamic corrosion experiments.

5600, USA) using Al Kα radiation (300 W) for excitation. Before recording the spectra, 4 nm of each surface was sputtered away in order to remove contamination. Sputtering was performed by means of Ar^+ ions at 3.5 kV with a sputter rate of 3.9 nm/min (calibrated with SiO_2). The binding energy of the target elements was determined at a pass energy of 23.5 eV with a resolution of 0.2 eV and a take-off angle of the emitted photoelectrons of 45°. The binding energy of the C1s signal at 284.8 eV was used in order to correct the spectra for charging. Additionally Fourier transform infrared spectroscopy (FTIR, Nicolet 6700, Smart iTR, Thermo Fisher Scientific) was carried out for further surface characterisation of the corroded and uncorroded specimen. Here, the ATR-D (attenuated total reflection) method was applied using a diamond element. Transmission and extinction spectra were collected in order to make a statement about the formed species and their relative amounts on the surface, respectively. Further characterisation of the alloy surface was performed by applying scanning electron microscopy (SEM, FEI Quanta 450) of the embedded and prepared cross-sections. The backscattered electron mode (BSE) allowed for improved elemental contrast. The outer surfaces of

Table 2
Summary and conditions of the dynamic corrosion experiments in vacuum dried eutectic LiCl–KCl–CsCl salt.

Alloy	Temperature, °C	Duration of experiment, h	Maximum depth of corrosion, μm	Standard deviation from two experiments, μm
X2CrNi18–9	400	3	34	
	500	3	24	
	600	3	37	
X6CrNiTi18–10	400	1	0	
		3	0	
		9	0	
		27	0	
	500	1	0	
		3	0	
		9[a]	56.5	8.5
		27[a]	42.4	27.9
	600	1	11.2	
		3[a]	30.5	4.8
		9	65.6	
		27[a]	51	10.4
CMSX-4	800	3	5[b]	

Experimental conditions: 50.6 LiCl–22.5 KCl–26.9 CsCl (mol-%); Ar 4.6 at 1 atm; 300 rpm.
[a] Second corrosion experiment was performed.
[b] No intergranular corrosion.

the three embedded samples per metallographic specimen were scanned and evaluated with respect to the deepest corrosion attack, measuring the pit depth perpendicular to the outer surfaces. By means of additional optical microscopy (Zeiss Axiophot, equipped with a Nikon digital camera DXM 1200), the surfaces of the corroded specimens were investigated.

3. Results

3.1. Evaporation

TGA experiments were carried out on a LiCl–KCl–CsCl mixture (50.6 mol-% – 22.5 mol-% – 26.9 mol-%). Weight loss as a function of temperature is shown in Fig. 2. No remarkable weight change occurs up to 100 °C. Obviously physically bound water is purged successfully during drying. The mass loss caused by evaporation increases remarkably above 600 °C. The results prove that a Liquid Salt Cooling process could be possible at ambient pressure.

3.2. Corrosion attack

The corrosion experiments of the present study were performed in Ar at ambient pressure. The test temperature for the steels is limited to a maximum of 600 °C as no higher temperatures are expected for the containment and holding devices in the casting furnace. The CMSX-4 superalloy, representing the material of the casting, is investigated at 800 °C. Normally the casting is protected from attack by the cooling liquid by the ceramic shell. It might happen though, that the mould cracks while being immersed into the cooling bath and the cooling liquid enters the crack and reacts with the metal surface because of the hydrostatic pressure in the bath.

For the low carbon stainless steel, corrosion experiments were performed for 3 h at 400, 500, and 600 °C. The light microscopic top-view images and the corresponding cross-sectional SEM micrographs of the corroded specimens are given in Fig. 4a–c. In addition, the maximum penetration depth due to intergranular corrosion is labelled in the SEM micrographs. As shown, the order of magnitude of the corrosion attack for all three temperatures is similar. However it appears that the strongest attack is observed at the highest experimental temperature at 600 °C. Furthermore, some additional phases are visible in the material. EDX-measurements indicate they are sulphides and oxides related to impurities in the steel. Due to the poor performance of X2CrNi18–9 it was decided to discontinue the experiments early on.

For the Ti-stabilised stainless steel, more detailed corrosion experiments were performed for 1 h, 3 h, 9 h and 27 h at 400 °C, 500 °C, and 600 °C, respectively (see Fig. 5a–f). It is worth mentioning that there was no appreciable change in weight and diameter observed for any of the experimental conditions. Therefore, the determination of the corrosion depth measured from the outer surface in the SEM analysis is legitimate, even though the investigation revealed local attack to the surface (e.g., Fig. 5f). The light microscopic top-view images and the corresponding cross-sectional SEM micrographs of the 1 h and 3 h investigated specimens are given in Fig. 5a–f. After 1 h and 3 h at 400 °C (Fig. 5a and b, respectively), only a very thin layer of corrosion products can be observed by light microscopic top-view images. In addition no intergranular corrosion takes place. After 1 h and 3 h at 500 °C (Fig. 5c and d, respectively) the thickness of the covering layer steadily increases (layer thickness in the range of 0.2–1 μm) but still no intergranular corrosion is detected. Further increase in temperature and time (Fig. 5e and f) leads to severe intergranular corrosion. For the stainless steel X6CrNiTi18–10, the temperature dependent corrosion data with respect to time is summarised in Fig. 6. In comparison to the lower temperature experiments, corrosion started immediately at 600 °C.

In addition to the two different stainless steels, corrosion experiments on a CMSX-4 Ni-base superalloy were performed for 3 h at 800 °C. The light microscopic top-view image and the corresponding cross-sectional SEM micrograph of the corroded specimen are given in Fig. 7. The molten salt causes uniform corrosion with a corrosion depth of approximately 5 μm. Intergranular corrosion is not observed. The results of the corrosion attack investigation are summed up in Table 2.

3.3. Surface analysis

XPS spectra of the corroded Ti-stabilised steel surfaces allow for identification of the corrosion products. In Fig. 8, XPS spectra of the characteristic Cr 2p (Fig. 8a) and Ni 2p peaks (Fig. 8b) are illustrated for the uncorroded polished sample and the specimens after 1 h at 400 °C and 3 h at 600 °C. Increasing exposure temperature and time results in a remarkable decrease of the Cr 2p peaks but, on the contrary, a strong decrease and reincrease of the Ni 2p peaks. The binding energies of the individual Cr 2p peaks (Fig. 8a) are within approximately 576.4–579.8 eV. Therefore, they can be ascribed to

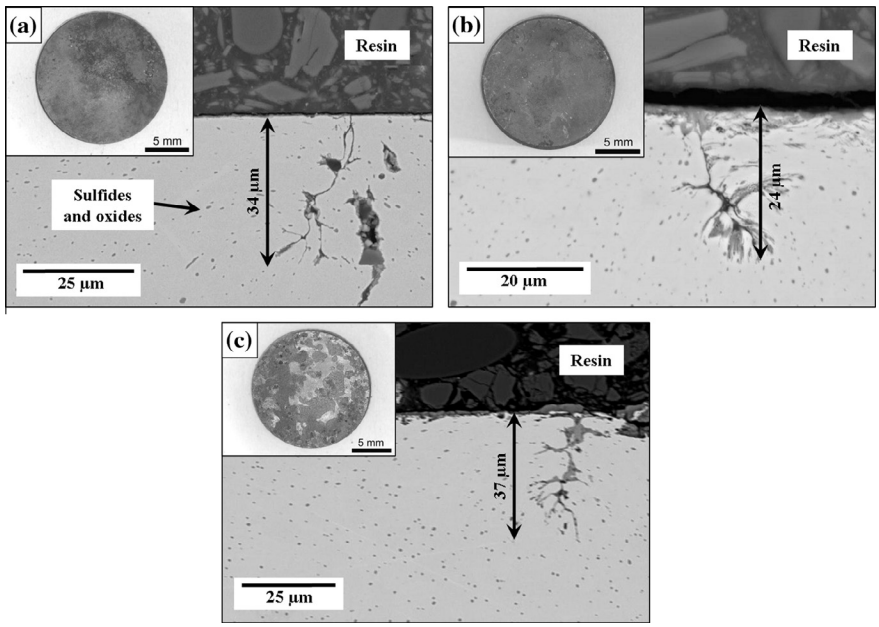

Fig. 4. Light microscopic top-view images and the corresponding cross-sectional SEM micrographs of the corroded low-carbon stainless steel X2CrNi18–9 after 3 h at 400 °C (a), 500 °C (b), and 600 °C (c). The maximum penetration depth of the intergranular corrosion is labelled in the SEM micrographs.

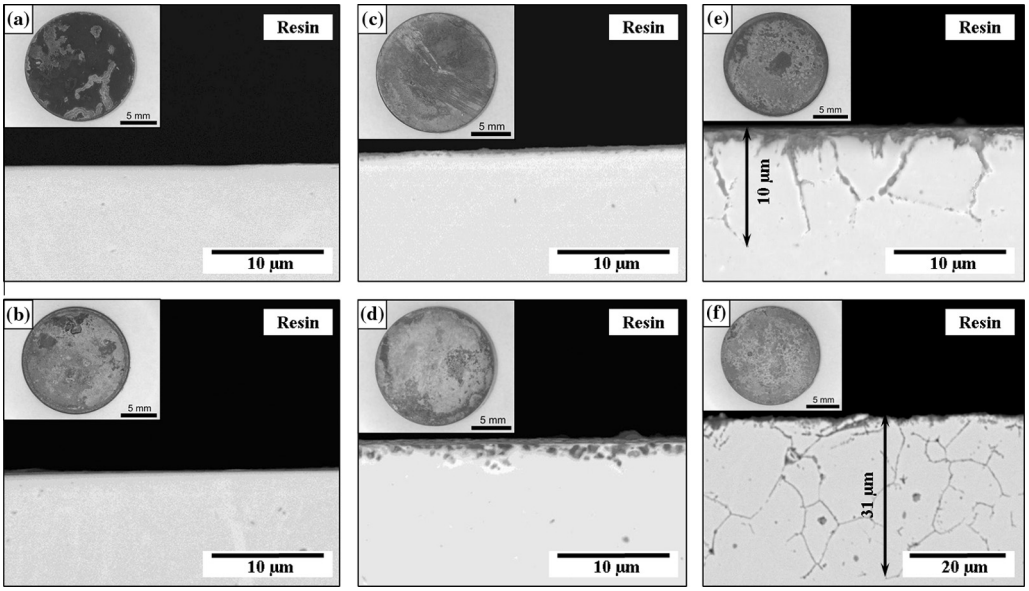

Fig. 5. Light microscopic top-view images and the corresponding cross-sectional SEM micrographs of the corroded Ti-stabilised stainless steel X6CrNiTi18–10 after 1 h at 400 °C (a), 3 h at 400 °C (b), 1 h at 500 °C (c), 3 h at 500 °C (d), 1 h at 600 °C (e), and 3 h at 600 °C (f). The maximum penetration depth of the intergranular corrosion is labelled in the SEM micrographs.

Cr_2O_3, based on the handbook of X-ray photoelectron spectroscopy [18]. The Ni 2p peaks of the corroded specimens (Fig. 8b) are located between approximately 855.3–857.5 eV and hence can be ascribed to $NiCl_2$. However, the signal of the sample corroded for 1 h at 400 °C is quite weak. Furthermore, it is very likely that the strong XPS signal of the uncorroded sample may be mainly due to the presence of an initial thin NiO layer which usually forms at ambient conditions in addition to Cr_2O_3. This explains the slight shift of the peak to lower binding energies. The assumption can be confirmed by the results from additional FTIR spectra of the corroded and uncorroded Ti-stabilised steel surfaces (see Fig. 9a and b). The spectra allow for better identification of the corrosion products which form at high temperatures. Characteristic chloride peaks are located between approximately 850 and 550 cm^{-1}. In Fig. 9a, the chloride peaks of the uncorroded sample and the specimen corroded for 1 h at 400 °C are comparable, whereas the peak of the sample after 3 h at 600 °C is significantly stronger. On the basis of Fig. 9b, very low amounts of chlorides can be found on the uncorroded specimen (presumably due to contamination) and on the specimen after 1 h at 400 °C, but significant amounts can be found on the sample corroded for 3 h at 600 °C. The observed noise at wave numbers of around 1500 cm^{-1} and between 4000 and 3500 cm^{-1} can be ascribed to undesired incidence and emission of light caused by the experimental set-up. Between approximately 2400 and 2000 cm^{-1}, a typical CO_2 absorption peak can be identified which originates from the surrounding air.

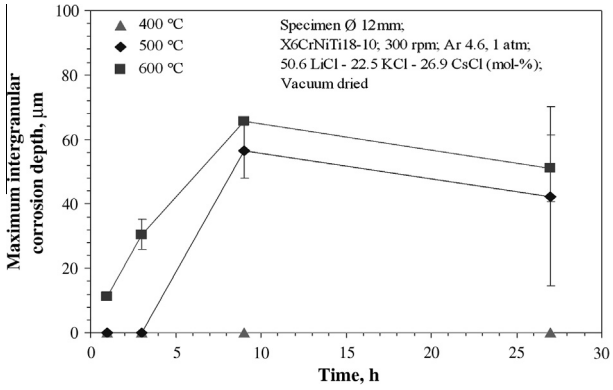

Fig. 6. The temperature dependent maximum intergranular corrosion depth of the Ti-stabilised stainless steel X6CrNiTi18–10 plotted against time. The experiments are conducted for 1, 3, 9, and 27 h at 400, 500, and 600 °C in vacuum dried 50.6 LiCl–22.5 KCl–26.9 CsCl (mol-%) salt under Ar 4.6 atmosphere. The rotation speed was 300 rpm (values with error bars were calculated from two different corroded samples and values without error bars from one corroded sample. Out of each corroded sample, three different cross-sections were prepared for evaluation).

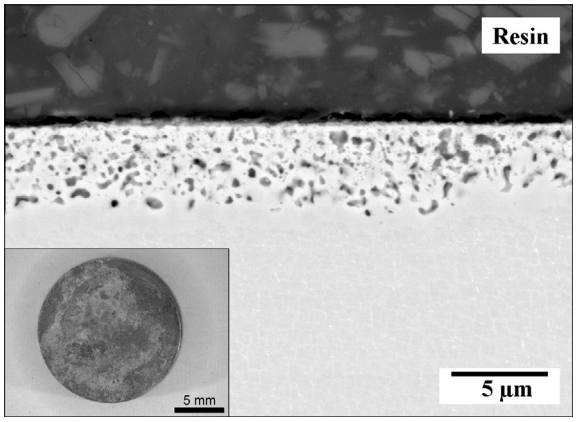

Fig. 7. Light microscopic top-view image and the corresponding cross-sectional SEM micrograph of the corroded CMSX-4 Ni-base superalloy after 3 h at 800 °C.

4. Discussion

The low-carbon stainless steel reveals inferior corrosion resistance in molten salt compared to the Ti-stabilised stainless steel and the CMSX-4 Ni-base superalloy. The reduced carbon content in the stainless steel does not lead to an improved resistance against intergranular corrosion, which is commonly associated with the formation of chromium carbides at the grain boundaries. Instead, intergranular corrosion can be observed at all three test temperatures (400, 500, and 600 °C). According to optical microscopy (see Fig. 4a–c), even partial dissolution of the surface and therefore accelerated corrosion can be observed after 3 h at 600 °C.

The common oxidants in molten salts, which accelerate corrosion, are O_2, H_2O, H^+, and OH^- [10]. The presence of oxygen and water in the molten salt can be related to insufficient salt drying, atmospheric contact of the salt prior to the experiment, and dissolution of oxygen and water vapour into the molten salt during the corrosion tests. Furthermore, water may dissociate into H^+ and OH^-, and Cl_2 can be present in the molten salt after reacting with oxygen [19]:

$$2Cl^- + \frac{1}{2}O_{2(g)} \leftrightarrow Cl_{2(g)} + O^{2-} \quad (4.1)$$

Cl_2 can also be formed as a consequence of Cl^- reaction with the initially formed Cr_2O_3 at the outer surface of the steel [20]:

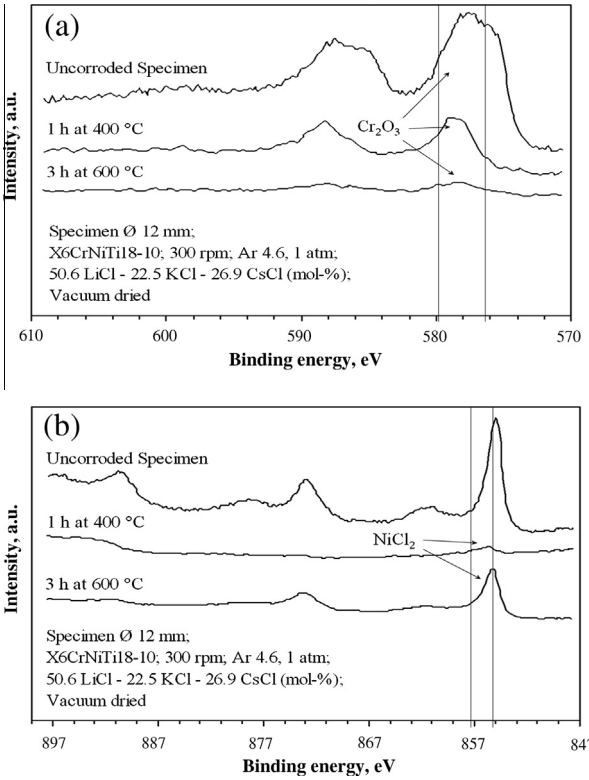

Fig. 8. XPS measurements on the surface of the Ti-stabilised stainless steel X6CrNiTi18–10 before corrosion, after 1 h at 400 °C, and after 3 h at 600 °C. (a) Characteristic Cr- and (b) characteristic Ni-peaks. The corrosion experiment was performed in vacuum dried 50.6 LiCl–22.5 KCl–26.9 CsCl (mol-%) salt under Ar 4.6 atmosphere. The rotation speed was 300 rpm.

$$8Cl^- + 2Cr_2O_{3(s)} + 5O_{2(g)} \rightarrow 4CrO_4^{2-} + 4Cl_{2(g)} \quad (4.2)$$

Assuming sufficiently high chlorine partial pressure and low oxygen partial pressure at the interface metal/oxide, penetration of chlorine through the oxide scale towards the base material may result in the formation of metal chlorides [21], such as:

$$Fe_{(s)} + Cl_{2(g)} \rightarrow FeCl_{2(s)} \quad (4.3)$$
$$Cr_{(s)} + Cl_{2(g)} \rightarrow CrCl_{2(s)} \quad (4.4)$$
$$Ni_{(s)} + Cl_{2(g)} \rightarrow NiCl_{2(s)} \quad (4.5)$$

The driving force for chlorine to penetrate the surface layer is the thermodynamic stability of the metal chlorides at sufficiently high chlorine partial pressure and low oxygen partial pressure, whereas the metal is not stable under such conditions [21,22].

The formed metal chlorides may evaporate steadily and diffuse in outward direction, e.g., due to cracks and pores. Subsequently, in regions with sufficient oxygen partial pressure (at the interface oxide/melt), a conversion into oxides may occur according to Refs. [21,23]:

$$3FeCl_{2(g)} + 2O_2 \rightarrow Fe_3O_{4(s)} + 3Cl_{2(g)} \quad (4.6)$$
$$2FeCl_{2(g)} + 1.5O_2 \rightarrow Fe_2O_{3(s)} + 2Cl_{2(g)} \quad (4.7)$$
$$2CrCl_{2(g)} + 1.5O_2 \rightarrow Cr_2O_{3(s)} + 2Cl_{2(g)} \quad (4.8)$$
$$2CrCl_{3(g)} + 1.5O_2 \rightarrow Cr_2O_{3(s)} + 3Cl_{2(g)} \quad (4.9)$$
$$NiCl_{2(g)} + 0.5O_2 \rightarrow NiO_{(s)} + Cl_{2(g)} \quad (4.10)$$

This process is known as a "chlorination–oxidation cycle" or "active oxidation", since no dense and protective scale (passivation) is formed [24,25]. The presented reactions, including the oxidation of chloride to chlorine, are strongly temperature dependent. Investigations on a Cr/Mo-containing steel between 450 and 650 °C [20] showed that below approximately 450 °C, chloride

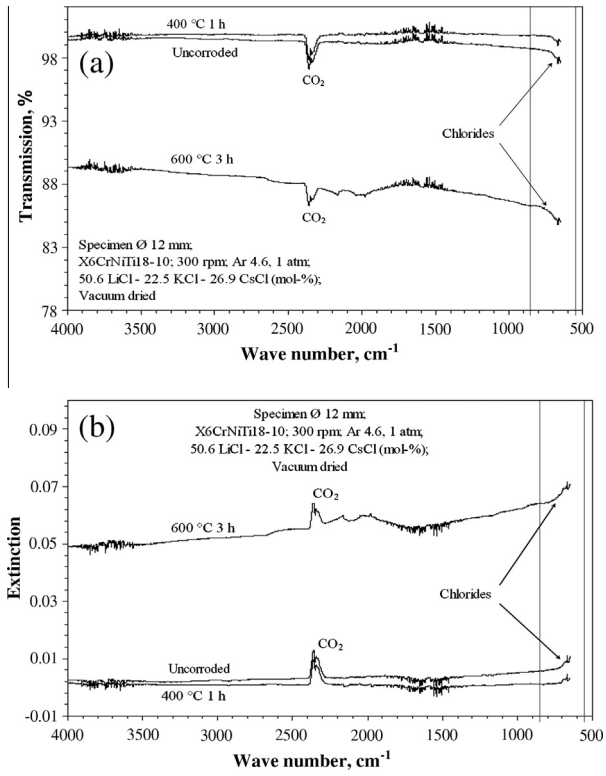

Fig. 9. FTIR spectra on the surface of the Ti-stabilised stainless steel X6CrNiTi18–10 before corrosion, after 1 h at 400 °C, and after 3 h at 600 °C. (a) Transmission spectrum and (b) extinction spectrum. The corrosion experiment was performed in vacuum dried 50.6 LiCl–22.5 KCl–26.9 CsCl (mol-%) salt under Ar 4.6 atmosphere. The rotation speed was 300 rpm.

induced active oxidation can be neglected, since almost no chlorine and therefore metal chlorides are formed. Above this temperature, active oxidation is highly increased leading to severe corrosive attack of the material. Furthermore, the presence of Cl_2 may lead to a preferential attack of chromium carbides at the grain boundaries according to Ref. [26]:

$$Cr_7C_{3(s)} + 7Cl_{2(g)} + 3O_2 \rightarrow 7CrCl_2 + 3CO_{2(g)} \quad (4.11)$$

$$Cr_{23}C_{6(s)} + 23Cl_{2(g)} + 3O_2 \rightarrow 23CrCl_2 + 6CO_{(g)} \quad (4.12)$$

$$Cr_{23}C_{6(s)} + 23Cl_{2(g)} \rightarrow 23CrCl_2 + 6C_{(s)} \quad (4.13)$$

For this reason, no chromium or carbon enrichment is detected at the grain boundaries of the investigated steels by supplemental EDX measurements. Furthermore, the produced $CrCl_2$ contributes to the already mentioned "chlorination–oxidation cycle".

The addition of stabilising elements, such as Ti, Zr, Hf or Ta to austenitic steels is reported to reduce intergranular corrosion [27]. The formation of titanium carbides at the grain boundaries is very likely the reason for the improved resistance of the Ti-stabilised stainless steel against intergranular corrosion below 600 °C. On the other hand, Ti-free stainless steel reveals enhanced susceptibility to corrosion. The formation of chromium carbides instead of titanium carbides weakens the initially formed Cr_2O_3 passivation layer and leads to chromium depletion in the surrounding of the grain boundaries. XPS and FTIR results of the investigated Ti-stabilised steel confirm the proposed theory, since no intergranular corrosion occurs for short exposure times at 400 °C (and 500 °C) due to a sufficiently protective Cr_2O_3 layer. However, the destruction of this passive layer by chlorides can be observed at higher temperatures, immediately at 600 °C and delayed at 500 °C, according to Eq. (4.2), accompanied by the formation of non-protective chloride compounds according to Eq. (4.5). $NiCl_2$ has a higher thermodynamic stability relative to NiO [21]. This is very likely the reason for the observed lack of NiO in our findings.

Fig. 6 shows that the rate of corrosion attack continuously decreases with increasing experimental time. This may be due to the generation of thicker corrosion products at the surface and the consumption of oxidants which both influence reaction kinetics. As already mentioned, four additional experiments were performed for verification of the 500 °C and 600 °C results. There is considerable scatter, which most likely results from the fact that the strongest intergranular attack was not necessarily found on the investigated polished section of the metallographic specimen.

The information obtained is important, as corrosion attack in fused salt is rather severe as soon as it is initiated. From that point of view, it does not appear reasonable to focus on structural material which is subject to ongoing intergranular corrosion. Based on the experiments, an initiation temperature for intergranular corrosion in X6CrNiTi18–10 may be assumed at approximately 500 °C.

In comparison to the investigated steels, the CMSX-4 Ni-base superalloy reveals superior corrosion resistance in molten salts (see Fig. 7). Here, no intergranular corrosion could be observed. This can be ascribed to the presence of stabilising elements, such as Ti, Ta, or Hf, and to sufficiently high amounts of Al and Cr, which may form protective species at 800 °C.

Operation of the corrosion test device revealed another type of low temperature corrosion attack due to evaporation of molten salt. After a rather short operation time and three additional downtime weeks, leakage became apparent at a thin walled bellow assembled in the setup. The bellow was made of X5CrNi18–10, which is a higher carbon containing variant of X2CrNi18–9. The bellow has not been in direct contact to the fused salt during the experiment but suffered from pitting corrosion. At reconditioning, corrosion on components made from copper and aluminium was additionally localised. As mentioned before, molten salt exhibits a high vapour pressure accompanied by evaporation at high temperature. As a consequence, there is condensation on cold parts of the setup. In this vein, white dust was observed to deposit on cool surfaces, in particular after experiments exceeding 500 °C. The dust liquefied after short exposure to air in accordance with the hygroscopy of chloride salt. Chlorine ions are well known to trigger pitting corrosion. In order to avoid damage in an industrial process like LSC, the controlled input of moisture is therefore not only essential for the high temperature but also for the low temperature persistence.

In summary, a LSC process appears to be feasible from the high temperature corrosion viewpoint. The material temperature in the casting device should be held below 500 °C; ideally it should not exceed 400 °C. Accordingly, the construction material X6CrNiTi18–10 appears to be applicable even in direct contact to molten salt. The second generation Ni-base superalloy CMSX-4 is only marginally affected by the molten salt, especially at short exposure time, which is typical for the solidification process.

5. Conclusions

1. The low-carbon stainless steel X2CrNi18–9 reveals severe intergranular corrosion in molten eutectic 50.6 LiCl–22.5 KCl–26.9 CsCl (mol-%), whereas the Ti-stabilised stainless steel X6CrNiTi18–10 is protected against intergranular corrosion by a Cr_2O_3 passive layer up to a temperature of approximately 500 °C and short exposure times. At higher temperatures and longer exposure times, the protective passive layer is degraded according to XPS measurements. The corrosion mechanism is

suggested to be based on a "chlorination–oxidation" mechanism already observed in other steels. This is supported by an increased amount of non-protective species, such as $NiCl_2$ on the corroded samples.

2. In comparison to the investigated stainless steels, the Ni-base superalloy CMSX-4 reveals only limited corrosion in the molten salt after exposure for 3 h at 800 °C.
3. As a consequence, a Ti-stabilised stainless steel may be an adequate structural material for novel casting facilities using liquid salt cooling up to exposure temperatures of approximately 400 °C and relatively short exposure times. The limitation of salt evaporation which causes a contamination of the equipment by certain salt species and a change in the thermophysical properties of the cooling bath remains a challenge for further development.

Acknowledgements

The authors are grateful for financial support from the German Research Foundation (DFG) in the framework of the collaborative research centre SFB/Transregio 103 (projects A5, B1 and WSP). Furthermore the authors would like to thank Sarah Höhn from the Institute for Surface Science and Corrosion (LKO) for the FTIR measurements.

References

[1] R.C. Briant, A.M. Weinberg, Nucl. Sci. Eng. 2 (1957) 797–803.
[2] R. Tamme, T. Bauer, J. Buschle, D. Laing, H. Müller-Steinhagen, W.-D. Steinmann, Int. J. Energy Res. 32 (2008) 264–271.
[3] K. Funatani, Met. Sci. Heat Treat. 46 (2004) 277–281.
[4] M. Lamm, R. Singer, Metall. Mater. Trans. A 38 (2007) 1177–1183.
[5] A.J. Elliott, T.M. Pollock, S. Tin, W.T. King, S.-C. Huang, M.F.X. Gigliotti, Metall. Mater. Trans. A 35 (2004) 3221–3231.
[6] A. Lohmüller, W. Eßler, J. Großmann, M. Hördler, J. Preuhs, R.F. Singer, in: Superalloys 2000 Proceedings of the 9. International Symposium on Superalloys, 2000, Seven Springs, PA, pp. 181–188.
[7] H. Moriyama, A. Sagara, S. Tanaka, R.W. Moir, D.K. Sze, Fusion Eng. Des. 39–40 (1998) 627–637.
[8] D.F. Williams, ORNL/TM-2006/69, Oak Ridge National Laboratory, Oak Ridge, Tennessee, 2006.
[9] L. Wang, T. Wallace, F. Hampel, J. Steele, Metall. Mater. Trans. B 27 (1996) 433–443.
[10] A. Nishikata, H. Numata, T. Tsuru, Mater. Sci. Eng. A 146 (1991) 15–31.
[11] G.J. Kipouros, D.R. Sadoway, J. Light Met. 1 (2001) 111–117.
[12] H.A. Laitinen, W.S. Ferguson, R.A. Osteryoung, J. Electrochem. Soc. 104 (1957) 516–520.
[13] Y.S. Li, M. Spiegel, S. Shimada, Mater. Chem. Phys. 93 (2005) 217–223.
[14] J.E. Indacochea, J.L. Smith, K.R. Litko, E.J. Karell, J. Mater. Res. 14 (1999) 1990–1995.
[15] G.Y. Lai, High-temperature Corrosion and Materials Applications, ASM International, Materials Park, Ohio, 2007.
[16] J.J. Demo, Metall. Trans. 5 (1974) 2253–2256.
[17] E. Aimen, C. Robelin, École Polytechnique Montreal, Canada: Personal communication.
[18] E. Renaud, C. Robelin, A.E. Gheribi, P. Chartrand, J. Chem. Thermodyn. 43 (8) (2011) 1286–1298.
[19] I.N. Ozeryanaya, Met. Sci. Heat Treat. 27 (1985) 184–188.
[20] H.J. Grabke, E. Reese, M. Spiegel, Corros. Sci. 37 (1995) 1023–1043.
[21] A. Zahs, M. Spiegel, H.J. Grabke, Corros. Sci. 42 (2000) 1093–1122.
[22] Y. Kawahara, Corros. Sci. 44 (2002) 223–245.
[23] A. Ruh, M. Spiegel, Corros. Sci. 48 (2006) 679–695.
[24] H.J. Grabke, M. Spiegel, A. Zahs, Mater. Res. 7 (2004) 89–95.
[25] B.P. Mohanty, D.A. Shores, Corros. Sci. 46 (2004) 2893–2907.
[26] R. Bender, M. Schütze, Mater. Corros. 54 (2003) 567–586.
[27] M. Terada, M. Saiki, I. Costa, A.F. Padilha, J. Nucl. Mater. 358 (2006) 40–46.